Chapter 4

Impacts of DC and RF Characteristics from the Association of Collector Doping Profiles and Deep Trench Structure

Preface

SiGe bipolar technology has become a popular fabrication process for wireless applications as its advantages of high quality, excellent stability and low cost. Including the applications in cellular phones, GPS and wireless LAN, SiGe bipolar technology associated with the DT isolation processes could provide high frequency and high isolation performances [1-2] while it increase the fabrication cost. While For low power applications, the cross-talk problems could be possibly suppressed or avoided by the optimizing the circuit orientation without adopting of the DT isolation process if the device characteristic deviations between the device with (denoted as DT devices) and without (denoted as non-DT devices) DT were well studied. However, limited information about this item has been published.

In this chapter, the electrical impacts due to the collector doping profile were continuously discussed with the involving of the deep trench (DT) isolation structure, which has been widely adopted in analogy and radio frequency integrated circuits for suppressing the signal cross-talk between devices and modules. First, the associated fabrication process flow of the SiGe HBT devices with DT technology were presented along with the corresponding modulation on collector profile. Such physical modulation on collector profile could alternate the DC and RF characteristics of the HBT devices could impact the circuit performance in several ways. It was the first time that the electrical impacts of the DT technology on HBT devices was reported and those discovery and physical origins could benefit the device and circuit designers to fabricate their products with even higher stability and performance.

4.0 Associated Physics

In this section, the associated physics, the base pushing out effect (Kirk effect) of a SiGe HBT device under high current driving operation was introduced. Figures 4.0.1 (a) and (b) illustrated the base-collector (BC) junction under low and higher current injection condition, respectively. Under some specific high current injection, the high-density hole current was injected into the collector and thus compensated the n-type atoms on the low concentration BC junction on the collector side. At the same time, the p-type charges of in the base space charge region would also be sharked for the charge neutralization basis. Such phenomenon was denoted as base pushing out effect (Kirk effect) and the specific current density level at which the Kirk effect took place was denoted as J_K in the following literature.

The deep trench isolation structure was fabricated subsequently to the selective collector implantation process. In this study, the HBT devices with (DT) and without DT structure (NDT) were designed in the fixed doping profile. However, several divergence between DT and NDT devices have been found in our study. In the following section, the electrical divergences would be discussed.

4.1 RF Characteristics of Deep Trench and Non-deep Trench Devices

In Figure 4.1.1, the basic parameters of the device RF performance, cutoff frequency f_T and maximum oscillation frequency f_{max} of devices with various collector doping levels, H-group (heavily doped), M-group (medium-doped) and L-group (light-doped) were illustrated. The traces with solid lines were f_T and dashed lines, f_{max}. The traces with open symbols were the devices without deep trench structure while the ones with closed marks, the DT devices. The H, M and L-group devices were marked in rectangular, triangular and diamond symbols.

In Fig. 4.1.1, the f_T-J_C relationships between the DT and NDT devices in M-Group were divergent to each other. Such behavior seemed to be unusual for devices designed in the fixed doping profiles. In addition, as the collector doping concentration decreased, such divergence was enlarged. On the other hand, as the collector doping level increased, such divergence shrank.

For further identifying the electrical divergence between DT and NDT devices, the DC characteristics of the devices were also pursued. In Figure 4.1.2, the measured values of breakdown voltage BV_{CEO} and the base-collector voltage C_{BC} of DT and NDT devices in H, M and L groups were illustrated. For wafer ID from 6 to 11, the devices were DT devices while from 12 to 17, NDT devices. The data in Fig. 4.1.2 were obtained from 48-points wafer mapping measurement and could be highly representative as the studying base in this research. From Fig. 4.1.2, the C_{BC} values of DT devices was higher than that of NDT devices in M-group and such C_{BC} divergence between DT and NDT devices were enlarged for L-group while for H-group, the divergence shrank. On the other hand, the values of the breakdown voltage BV_{CEO} of DT and NDT devices in the three groups exhibited the similar behavior observed in Figs 4.1.1 and 4.1.2.

In order to identify the physical origins of the behaviors observed in Figs 4.1.1 and 4.1.2, the popular process simulation tool SUPREM-4 has been adopted. The doping species, Phosphorus (P, as the selective collector implant layer (SIC) in n-epitaxy region) and Arsenic (As, as the n-type barrier layer, NBL) presented in the collector region were simulated for DT and NDT devices in L and H-groups and illustrated in Figure 4.1.3. In Fig. 4.1.3, both SIC and NBL profiles were wider than those in NDT devices. It could be highly possible that excess thermal has been introduced during the DT associated fabrication processes and then widen the profiles. Such profile widening resulting from the excess thermal during the DT technology approximately doubled the n-type carrier concentration at the BC junction edge on the collector side compared with the NDT devices in L-group illustrated in the inserted figure in Fig. 4.1.3. On the other hand, limited concentration increase at the BC junction edge on the collector side was observed for DT devices in H-group resulting from the higher SIC concentration level.

Based on the simulation results in Fig. 4.1.3, the behaviors in Figs. 4.1.1 and 4.1.2 could be demonstrated. First, the breakdown voltage values BV_{CEO} of DT devices were relatively lower than those of the NDT devices in L-group resulting from the SIC profile widening effect. At the mean time, the C_{BC} values of the DT devices exhibited relative lower values compared with those of the NDT devices in L-group resulting from the relatively higher electrical field in the space charge region. Second, the divergent electrical characteristics between DT and NDT devices in H-group in Figs 4.1.1 and 4.1.2 were limited resulting from the limited profile widening induced concentration modulation at the BC junction edge on the collector side. In other words, increasing the doping level of the SIC layer could successfully suppress the sensitivity of the electrical parameters (f_T-J_C, C_{BC} and BV_{CEO}) against the excess thermal induced NBL profile modulation during the DT fabrication.

In the subsequent sections, other critical performance factors, which could dominate the RF capability, were reported focused on the DT induced NBL profile modulation.

4.2 RF Noise Characteristics of Deep Trench and Non-deep Trench Devices

In this section, the key parameters, which could dominate the RF and noise characteristics including the minimum noise, figure NF_{min}, association gain G_{ass}, optimum source impedance Γ_{opt} for obtaining NF_{min}, input and output reflection coefficients (S_{11} and S_{22}) and forward transmission coefficient S_{21} would be discussed in accordance with the DT induced NBL profile modulation. It could provide the device and circuit designers to design their product further properly.

4.2.1 Impacts on Minimum Noise Figure and Association Gain

Figure 4.2.1 (a) and (b) illustrated the frequency dependency of minimum noise figure NF_{min} and association gain G_{ass} of DT and NDT devices in L and H-groups under V_{BE} 0.85 and 0.9 volts, respectively along with constant V_{BC} 1volt. The NF_{min}-freq and G_{ass}-freq traces were illustrated in solid and dashed lines in which the NDT and DT devices were illustrated in open and closed symbols, respectively. In Figs. 4.2.1 (a) and (b), the frequency dependent NF_{min} and G_{ass} of DT and NDT devices exhibited inconsistently from 1.8 to 10 GHz. On the other hand, in the H-group, the behavior divergence in between DT and NDT devices was not significant. It was straight forward that the values of the association gain were directly related to the behavior of the small signal forward current gain h_{fE} and thus the behavior of the cutoff frequency f_T. Similar behaviors of NF_{min} were also observed in Fig. 4.2.1 (a) and (b). NF_{min} could be illustrated in the following formula in terms of the device model parameters [3]:

$$NF_{\min} = 1 + \frac{r}{r_\pi}\left[1 + \frac{1}{\beta}\left(\frac{f}{f_T}\right)^2\right] + \sqrt{\frac{2r}{r_\pi}\left(1 + \frac{r}{2r_\pi}\right) + \frac{1}{\beta}\frac{2r}{r_\pi}\left(1 + \frac{r}{r_\pi}\right)\left(\frac{f}{f_T}\right)^2} \qquad (4.2.1)$$

Equation 4.2.1 were derived based on the high frequency noise model and chain-representation theorem. The frequency dependency of NF_{min} illustrated in Figs. 4.2.1 (a) and (b) could attribute to the term f/f_T in Eq. 4.2.1. Eq. 4.2.1 provided a direct relation between NF_{min} and f_T. Besides, the NF_{min} behaviors of DT and NDT devices in L and H groups observed in Figs. 4.2.1 (a) and (b) could directly attribute to the electrical modulation of f_T since the other factors in Eq. 4.2.1 were defined by the processes subsequent to DT associated processes.

In addition to the DT thermal induced modulation on the frequency dependency of NF_{min} and G_{ass}, the bias dependency of NF_{min} and G_{ass} could exhibit the similar behaviors. In Figures 4.2.1 (c) and (d), NF_{min} and G_{ass} values versus the collector currents of DT and DNT devices in L and H-groups at 2.4 and 5.8 GHz were illustrated, respectively. From Figs. 4.2.1 (c) and (d), the bias dependent characteristics of NF_{min} and G_{ass} for DT and NDT devices exhibited similarly while the divergence of NF_{min} and G_{ass} for DT and NDT devices in L-group grew with the collector current. Such phenomenon could be easily understood from the f_T-J_C relationships of DT and NDT devices in L-group illustrated in Figs. 4.1.1.

4.2.2 Impacts on Optimum Source Matching Point Γ_{opt}

In 4.2.1, the impacts of the DT associated excess thermal on the basic RF noise factors of an active device, minimum noise figure NF_{min} and association gain G_{ass} have been discussed. In this paragraph, the DT induced performance modulation on another important factor defining the RF noise of the device, the optimum source matching point Γ_{opt}, would be reported.

In Figures 4.2.2 (a) and (b), the frequency dependency of the normalized magnitude and angle of Γ_{opt} for DT and NDT devices in groups L and H were illustrated. Again, similar results could be observed in Figs. 4.2.3 (a) and (b). In order to obtained the physical origins, the optimum matching admittance $Y_{opt} = G_{opt} + B_{opt}$ and illustrated as follow [3]:

$$G_{opt} = \sqrt{\frac{G_n}{R_n} - (\frac{C_i}{R_n})^2} \quad .$$

$$B_{opt} = (\frac{C_i}{R_n})^2 \quad .$$

Where

$$R_n = \frac{T}{T_0}[r(1+\frac{n_c}{\beta}) + r_\pi \frac{n_c}{2\beta}] + r^2 G_n \quad .$$

$$G_n = \frac{T}{T_0}\frac{g_\pi}{2}[n_b + \frac{n_c}{\beta}(1+\frac{f^2}{f_T^2})] \quad .$$

$$C_i = -\frac{T}{T_0}\frac{n_c}{2\beta}\frac{f}{f_T} \qquad (4.2.2)$$

In Eq. 4.2.2, n_b and n_c illustrated the ideal factors of the BE and BC junction respectively. The optimum source matching point Γ_{opt} could be directly defined by Y_{opt} and thus G_{opt} and B_{opt}. T denoted as the ambient temperature in absolute unit. Similar to Eq. 4.2.1, the factors presented in Eq. 4.2.2 were defined by the processes subsequent to the DT associated process except for the cutoff frequency f_T. Once again, it was identified that the DT associated excess thermal could modulate the parameters Γ_{opt} which defined the input matching network of an amplifier by which the minimum noise figure could be obtained.

Furthermore, the bias dependency of the normalized magnitude and angle of Γ_{opt} were illustrated in Figure 4.2.2 (c) and (d) at 2.4 and 5.8 GHz, respectively. At higher collector current levels, the characteristic divergence between DT and NDT devices in

L-group grew while kept consistent for devices in H-group.

From the above discussion, it was demonstrated that increasing the doping concentration in the SIC layer, the divergence of the noise parameters could be suppressed as well. In the following paragraph, the DT induced impacts on the other RF parameters S_{11}, S_{21} and S_{22} of the HBT devices would be discussed

4.2.3 Impacts on Device S Parameters

In Figures 4.2.3 (a) and (b), the optimum source matching point Γ_{opt} and the output reflection coefficient S_{22} of DT and NDT devices in groups L and H were illustrated in a Smith plane from 50 M to 40 GHz under V_{BE} 0.85 and 0.9 volt, respectively. In the Smith plane, the DT induced modulation on Γ_{opt} for various devices could be observed more precisely and directly for circuit designers. It directly reflected how the DT associated process could impact the circuit performance if the L-group devices were adopted. Besides, significant divergence of S_{22} for NDT devices in L-group were discovered in Fig. 4.2.3 (a) and (b). Even for the DT and NDT devices in the H-group, more or less inconsistency could also be found. Based on the definition of the reflection coefficient, the collector profile could directly alternate the reflection coefficient S_{22} of a device. For this reason, finite inconsistency of S_{22} between DT and NDT devices could also be discovered in H-group. In Fig. 4.2.3 (b), significant divergence of Γ_{opt} between DT and NDT devices in L-group were found. It reflected again that the DT induced electrical modulation could be enlarged as the biasing current grew.

In Figure 4.2.3 (c) and (d), the input reflection parameter S_{11} and forward transmission coefficient S_{21} of DT and NDT devices in L and H groups under V_{BE} 0.85 and 0.9 volts were illustrated. From Figs. 4.2.3 (c) and (d), the input reflection coefficients S_{11} of the DT and NDT devices in L-group showed small inconsistency to each other while for the devices in H-group, the S_{11} values of DT and NDT devices agreed with each other. It could result from the finite reverse transmission values of the active devices S_{12} that blocked the incident wave from the output port. As a result, the values of S_{11} could reflected limited information from the output port so as to be relatively insensitive to DT associated thermal compared with S_{21} that could reflected the information along the signal path.

From the above discussion, it was demonstrated that the adoption of the DT technology in a designed circuit could failed to meet the simulation target if the device model did not included the DT associated excess thermal effect by which both RF and noise characteristics could be modulated. By heavily doping the collector region, the specific electrical properties could behave consistently while there still existed divergences in the devices parameters including S_{21}, S_{22}, Y_{21} and Y_{22} that could induced potential performance instability in RFIC design.

4.3 Linearity Characteristics and Power Capability of Deep Trench and Non-deep Trench Devices

The SiGe HBT devices could have great potential to fabricated large signal or power amplifier in analog and RF ICs because of their high driving capability. For higher power application, the linearity and output power could be the critical device indexes for meeting the circuit specs. In this section, the DT associated thermal induced modulation on the linearity factor, third order intersection point TOI, the power gain G_p and power added efficiency PAE for DT and NDT devices in L and H-groups would be discussed.

4.3.1 DT Associated Impact on TOI

In Figures 4.3.1 (a) and (b), the third order intersect point TOI of DT and NDT devices in L and H-groups under sweeping collector current density were illustrated at 2.4 and 5.8 GHz, respectively. From Figs. 4.3.1 (a) and (b), the TOI-J_C values of DT and NDT devices in L-group exhibited significant inconsistency to each other while in H-group, the DT and NDT devices, limited divergence was found. Furthermore, the characteristic divergence between DT and NDT devices in L-group grew as the operation frequency was increased from 2.4 GHz to 5.8 GHz. In order to evaluate the corresponding physical origins, the Voltarra approach [4] have been adopted in this research associated with the fundamental network theorem by which the TOI values could be linked to the cutoff frequency f_T.

$$OIP_3 \cong \sqrt{\frac{3}{4}}\,\frac{\left(\frac{w_T}{wR_S^*}\right)^{3/2}}{(G_{3HF}^2+G_{3IT}^2+\zeta)^{1/4}} \tag{4.3.1}$$

Where G_{3IT} and G_{3HF} were functions of device parameters including the low frequency current gain β, emitter resistance r_E, transconductance g_m, the source resistance R_S and the cutoff frequency w_T ($2\pi f_T$). In addition, the parameter ξ was simply a function of operation frequency along with r_E and R_S. Therefore, the excess thermal induced NBL profile modulation could also impact the behavior of device TOI through the cutoff frequency. Furthermore, the peak TOI values could take place near the current density at which the peak f_T took place as well resulting from the TOI cancellation created by the nonlinear transconductance and nonlinear storage charge in the transistor. As a result, The DT associated process could globally impact the electrical characteristics of the devices.

4.3.2 DT Associated Impact on G_p and PAE

Similar to the behavior discussed above in this chapter, the key index P_{OUT} and

PAE of a SiGe HBT for high power applications could be alternated by the DT associated impact. In Figures 4.3.2 (a) to (d), the power gain G_p and power added efficiency PAE of DT and NDT devices in L and H-groups. In L groups, the behavior divergence of P_{OUT} and PAE between DT and NDT devices could be even significant at higher operation frequency and higher bias current as well.

4.4 Conclusion

In this chapter, the deep trench associated impacts on device’s DC and RF performance have been reported and analyzed. Based on the theoretical and experimental results, the electrical behavior divergence could be efficiently suppressed by heavily implanting the collector region. For low power analog and RF application in which the signal cross talk issue could be less significant by carefully layout arrangement. As a result, high SIC concentration non-DT technology could be adopted for saving the fabrication cost and increasing the throughput without degrading the performance and stability of the products. However, the DT associated electrical modulation effects should be included in device model to reduce the IC design risk. The SPICE comparable model for predicting the DT corresponding effect could be valuable research topics.

Reference

[1] H. Yoshida, H., Suzuki and Y. Kinoshita, "An RF Process Using High f_{SR} Spiral Inductor with Premetal Deep Trenches and a Dual Recessed Bipolar Collector Sink", in *IEEE IEDM*, p.p. 851-854, 1998

[2] Cheon Soo Kim, Piljae Park and Joung-Woo Park, "Deep Trench Guard Technology to Suppress Coupling between Inductors in Si RF Ics", *IEEE MTT Digst*, p.p 1873-1876, 2001

[3] Guofu Niu, John D. Cressler and Shiming Zhang, "Noise-Gain Trasdeoff in RF SiGe HBT", *IEEE*, p.p 187-191, 2001

[4] Mani Vaidyanathan, "A theory of High Frequency Distortion in Bipolar Transistors", *IEEE Trans.* p.p. 448 – 461, Vol. 51, No. 2, 2003

Figures and Tables in Chapter 4

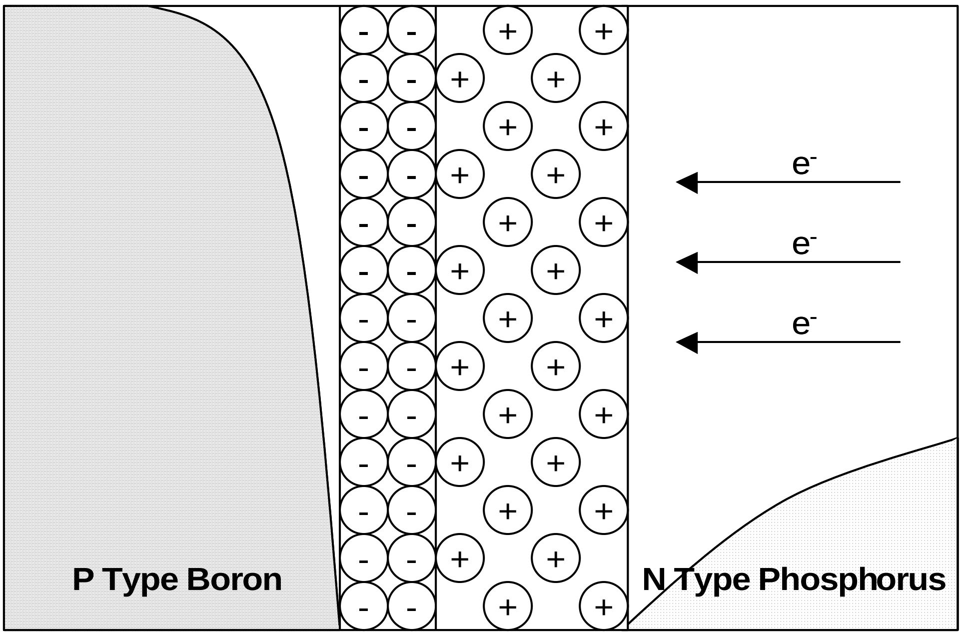

Electric current in the collector region under low current density condition

Figure 4.0.1 (a)

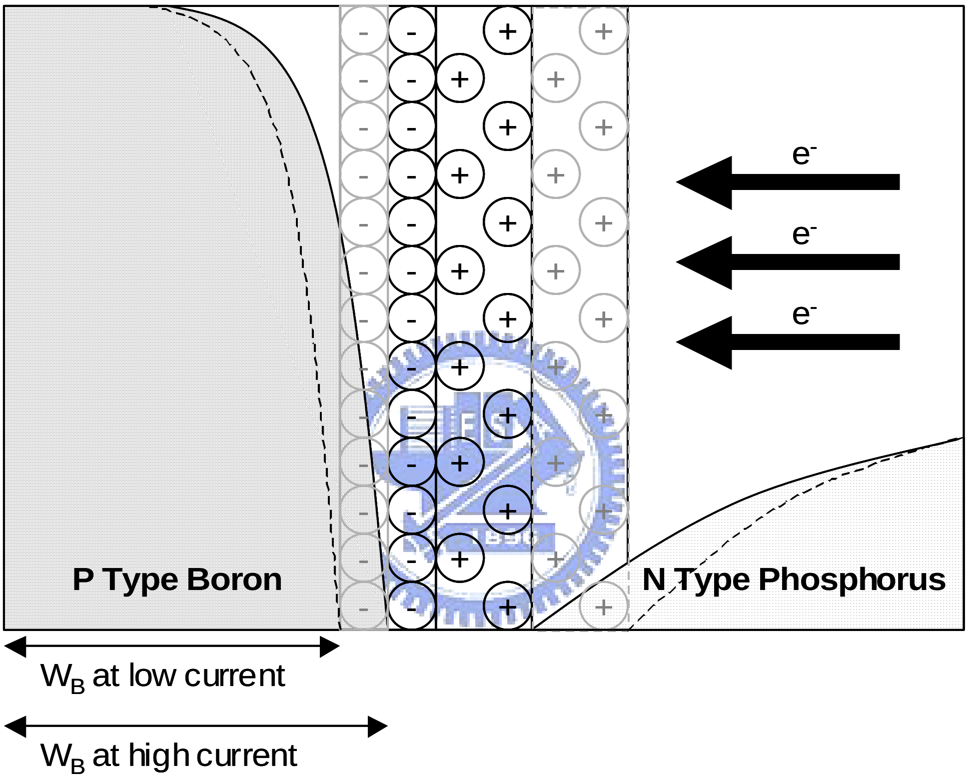

Electric current in the collector region under high current density condition

Figure 4.0.1 (b)

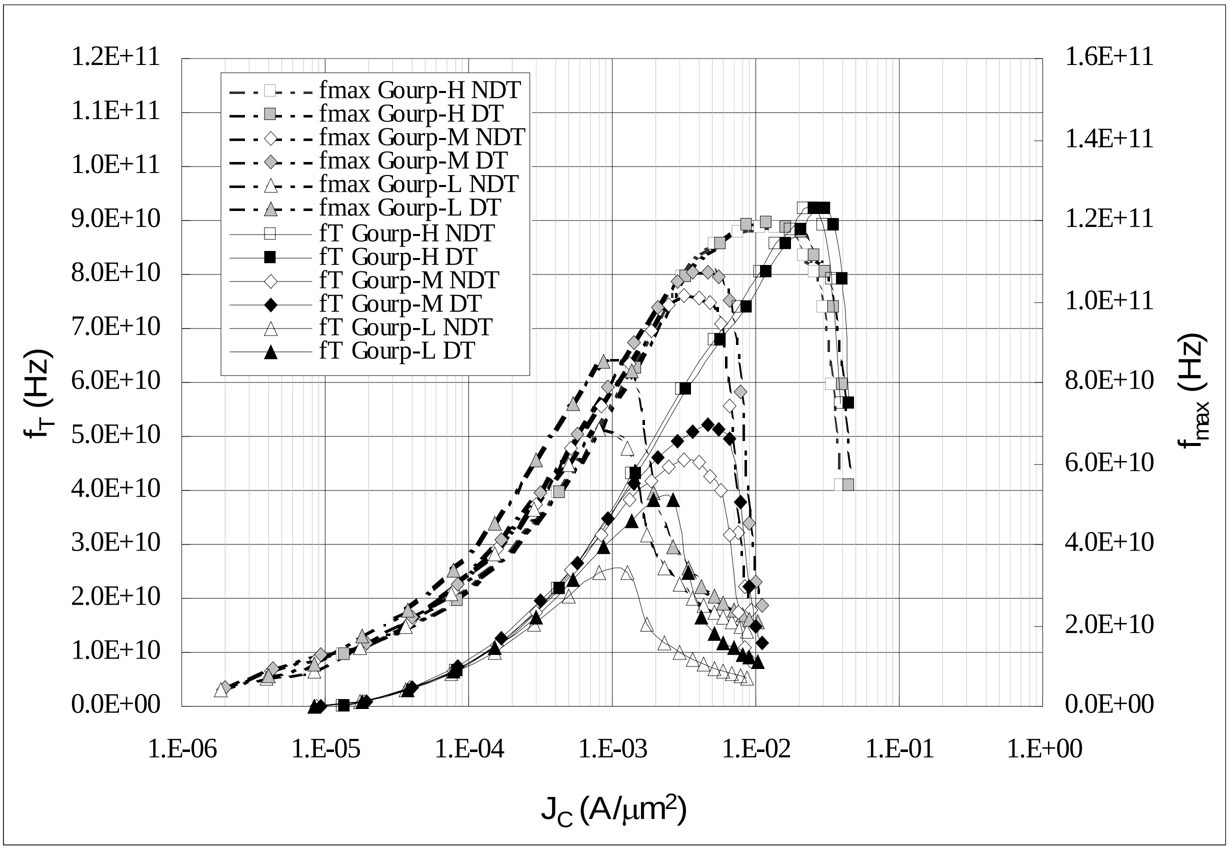

f_T-J_C and f_{max} -J_C measurement results of DT and NDT devices in H and L groups

Figure 4.1.1

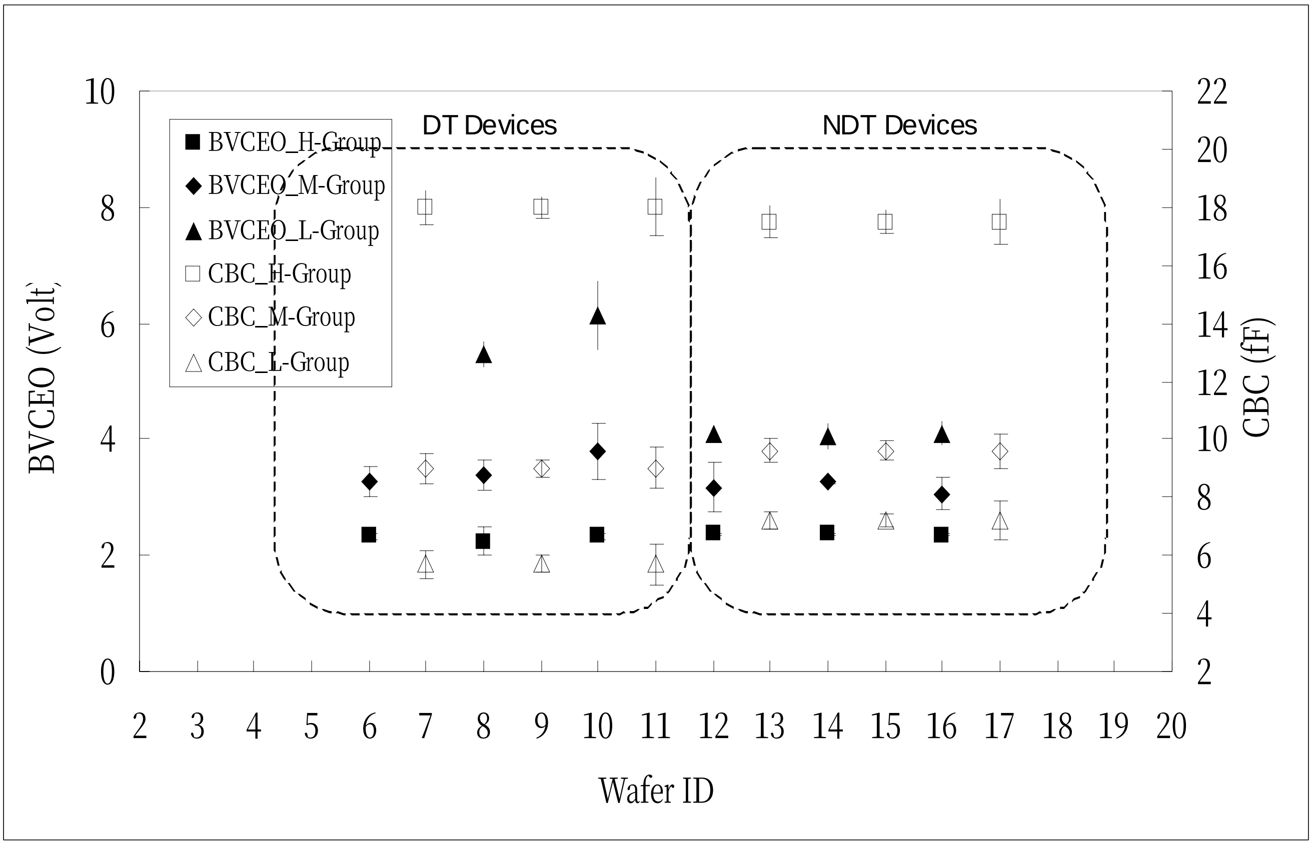

BV$_{CEO}$ and C$_{BC}$ measurement results of DT and NDT devices in H and L groups

Figure 4.1.2

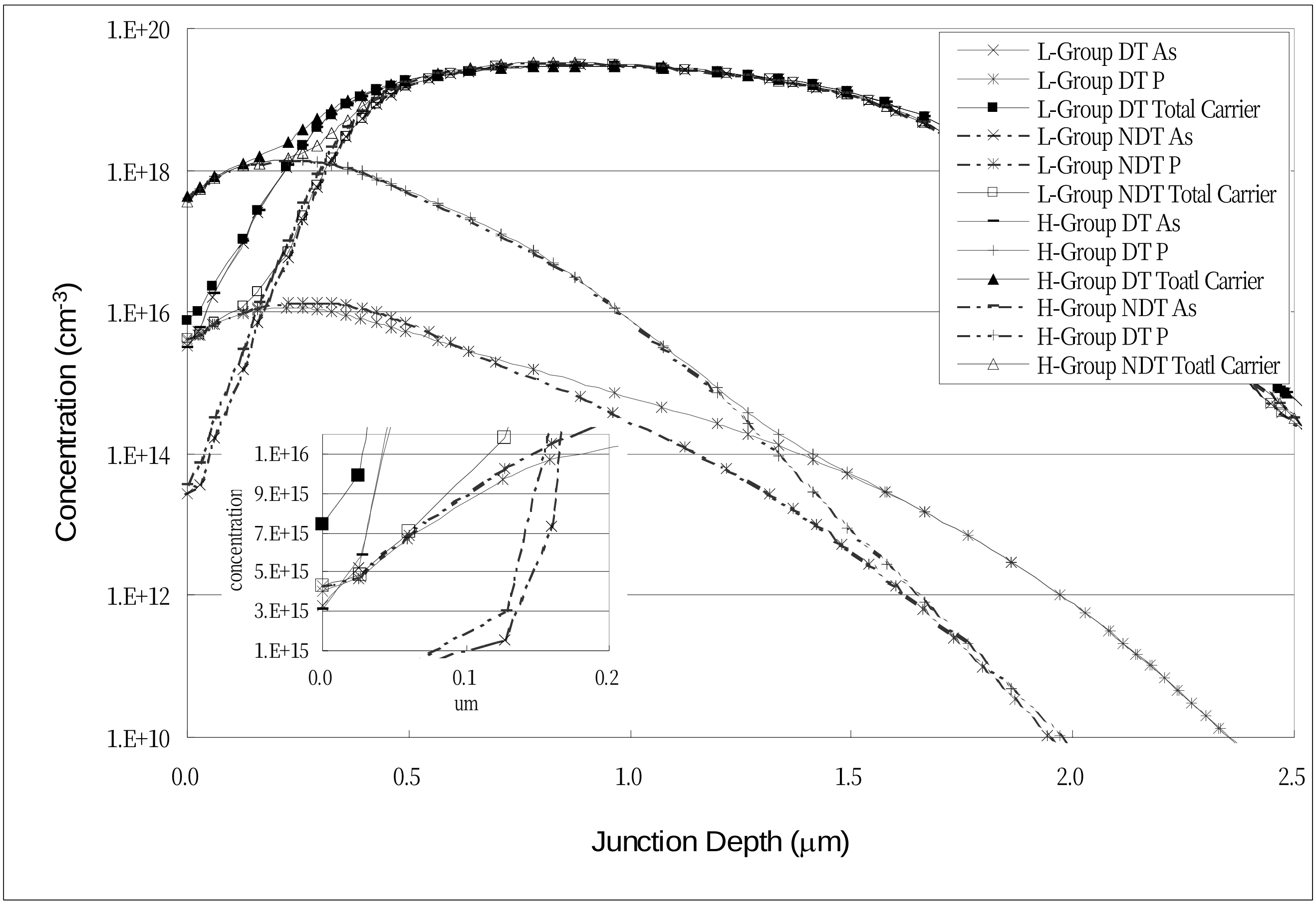

Doping concentration profile of phosphorus, arsenic and total carriers of DT and NDT devices in H and L groups

Figure 4.1.3

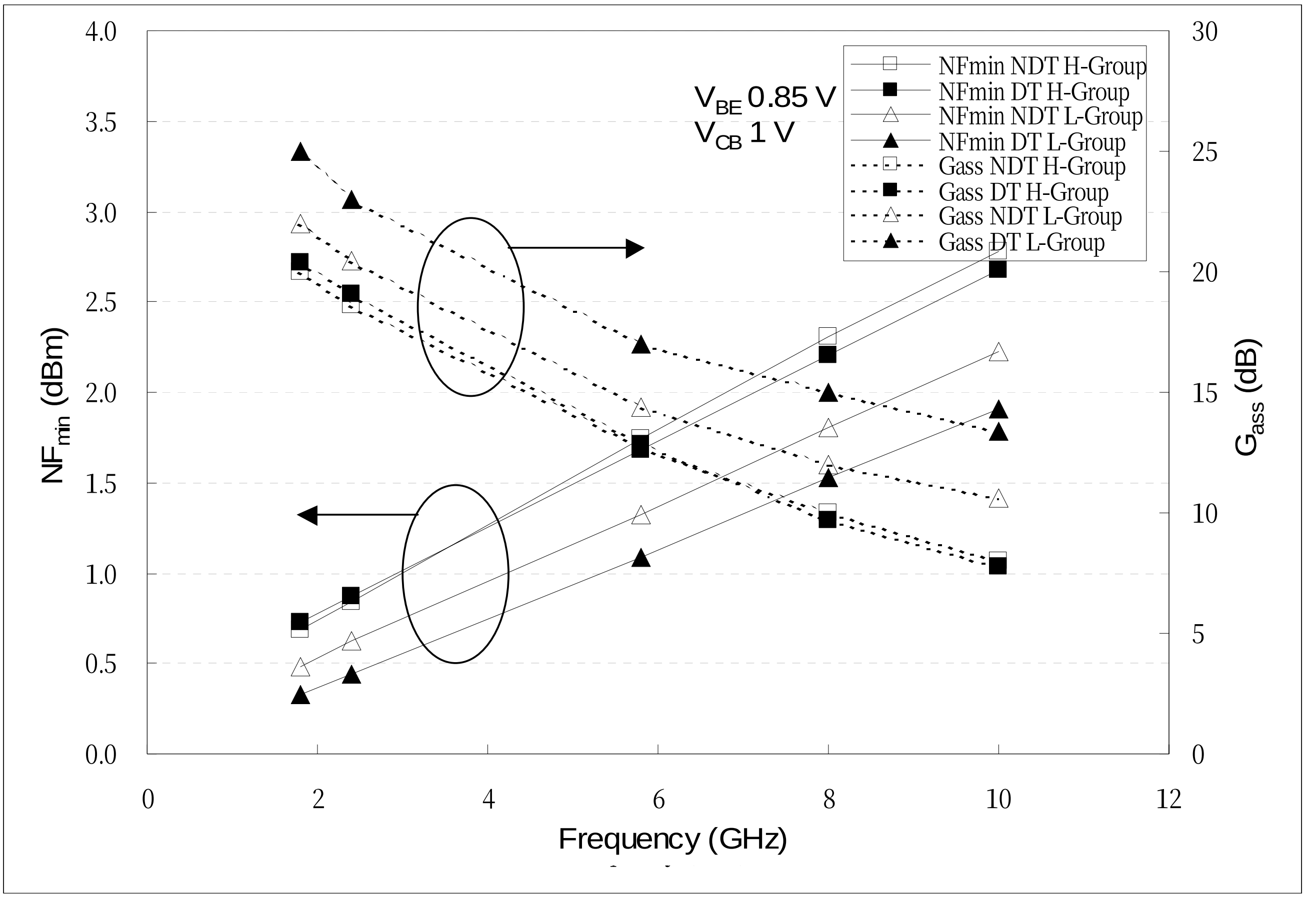

Minimum noise figure and association gain of DT and NDT devices in H and L groups versus operation frequency under V_{BE} 0.85 volt

Figure 4.2.1 (a)

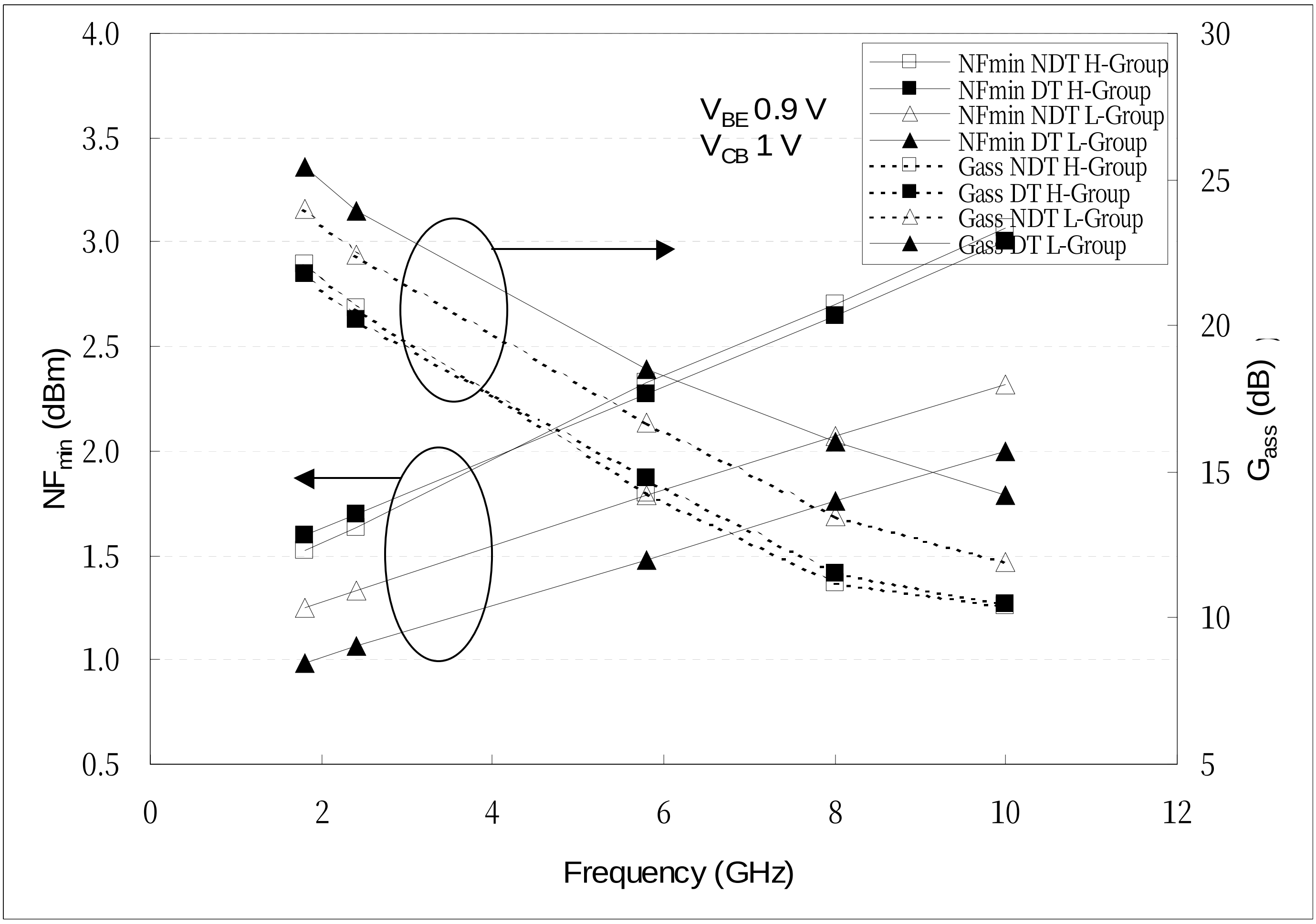

Minimum noise figure and association gain of DT and NDT devices in H and L groups versus operation frequency under V_{BE} 0.9 volt

Figure 4.2.1 (b)

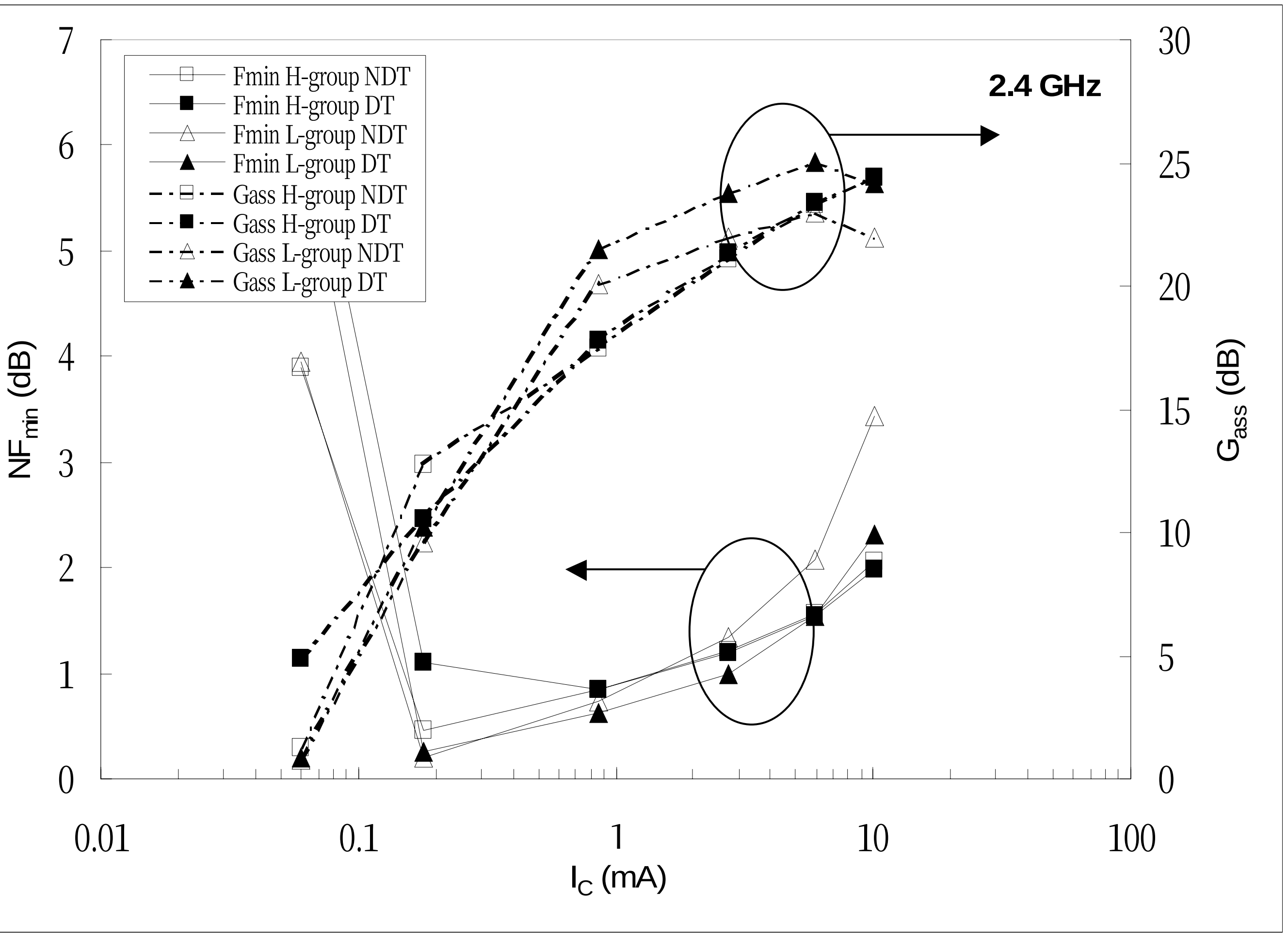

Minimum noise figure and association gain of DT and NDT devices in H and L groups versus operation current at 2.4 GHz

Figure 4.2.1 (c)

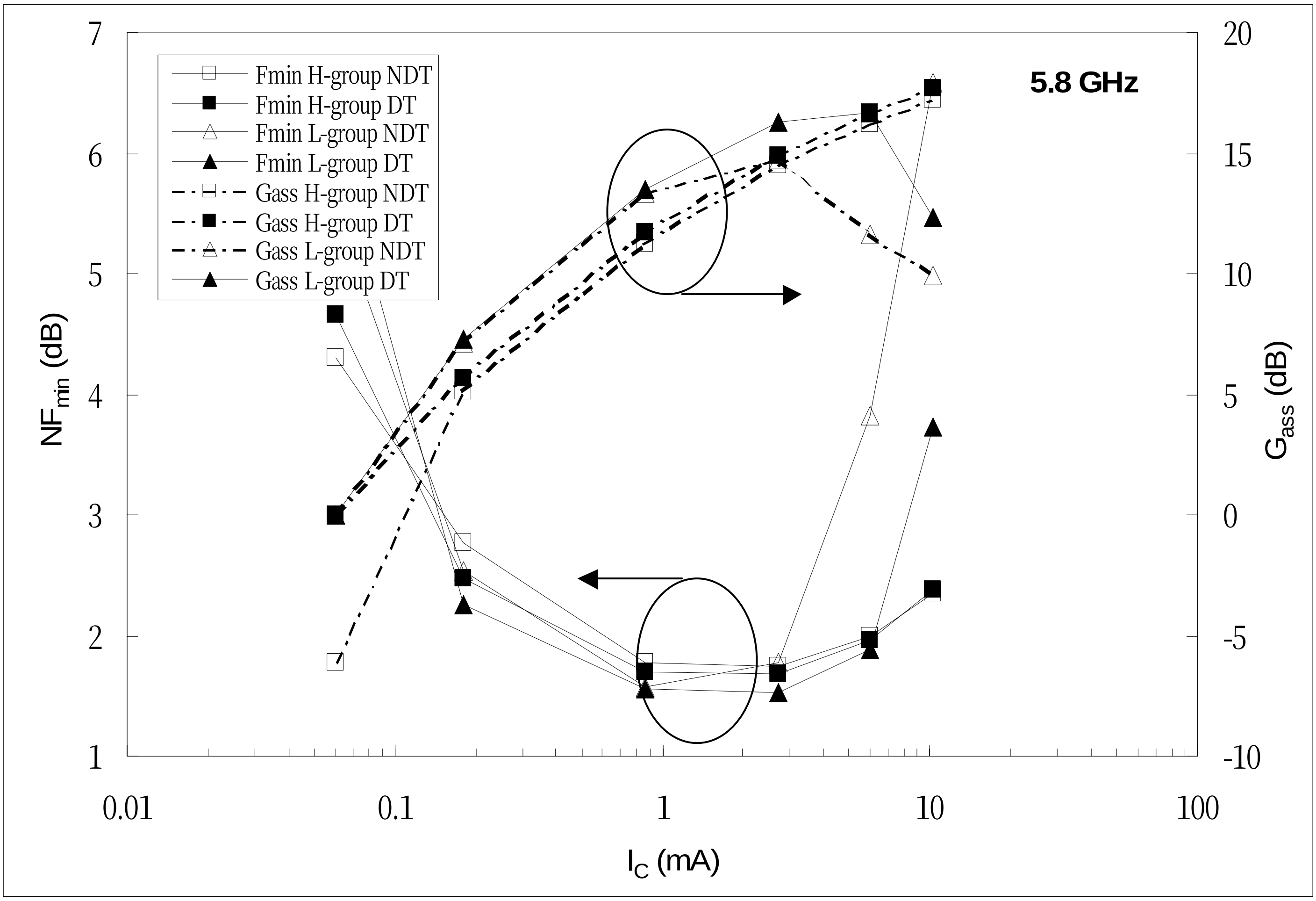

Minimum noise figure and association gain of DT and NDT devices in H and L groups versus operation current at 5.8 GHz

Figure 4.2.1 (d)

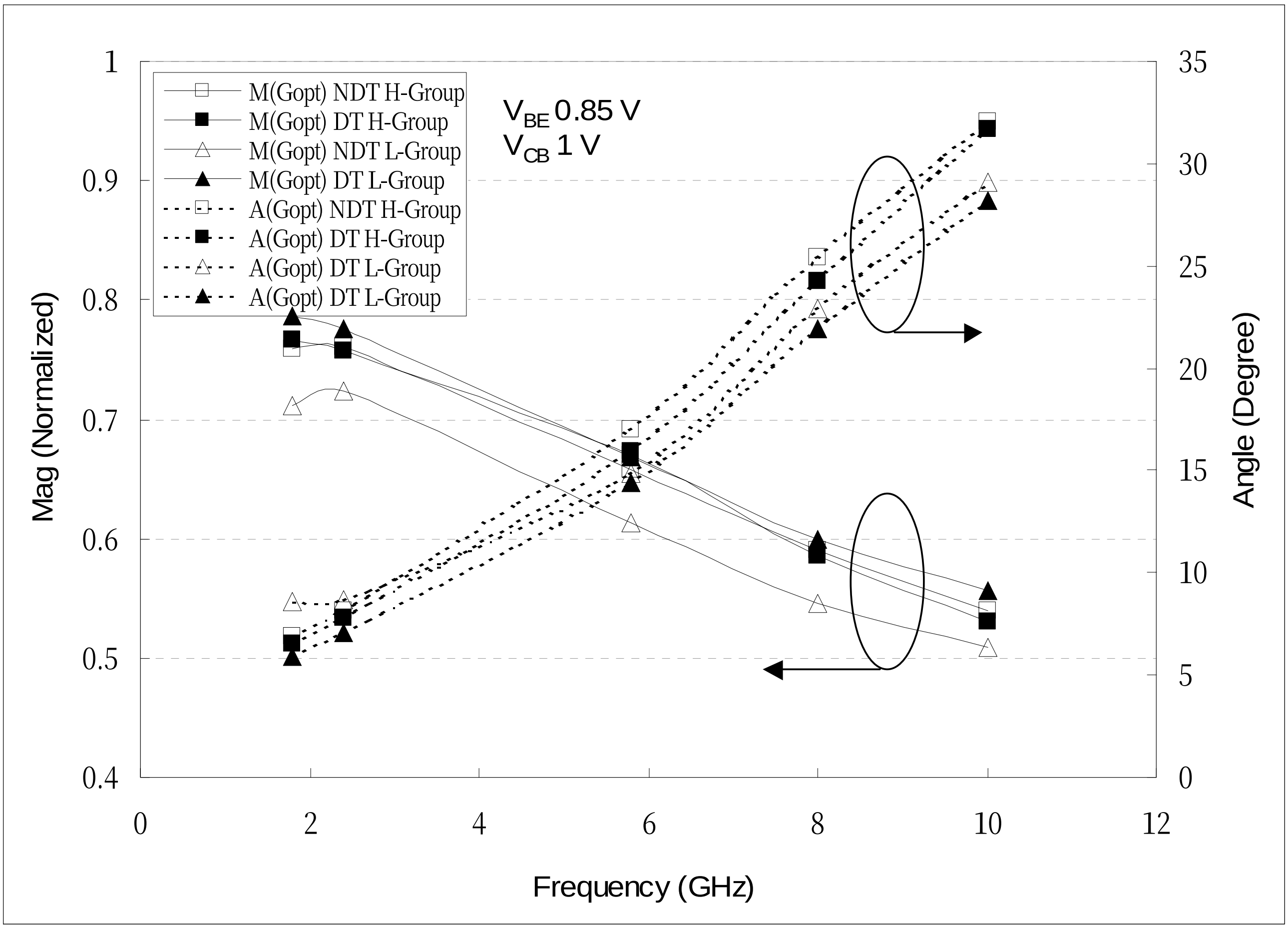

Magnitude and angle of Γ_{opt} of DT and NDT devices in H and L groups versus operation frequency at V_{BE} 0.85 volt

Figure 4.2.2 (a)

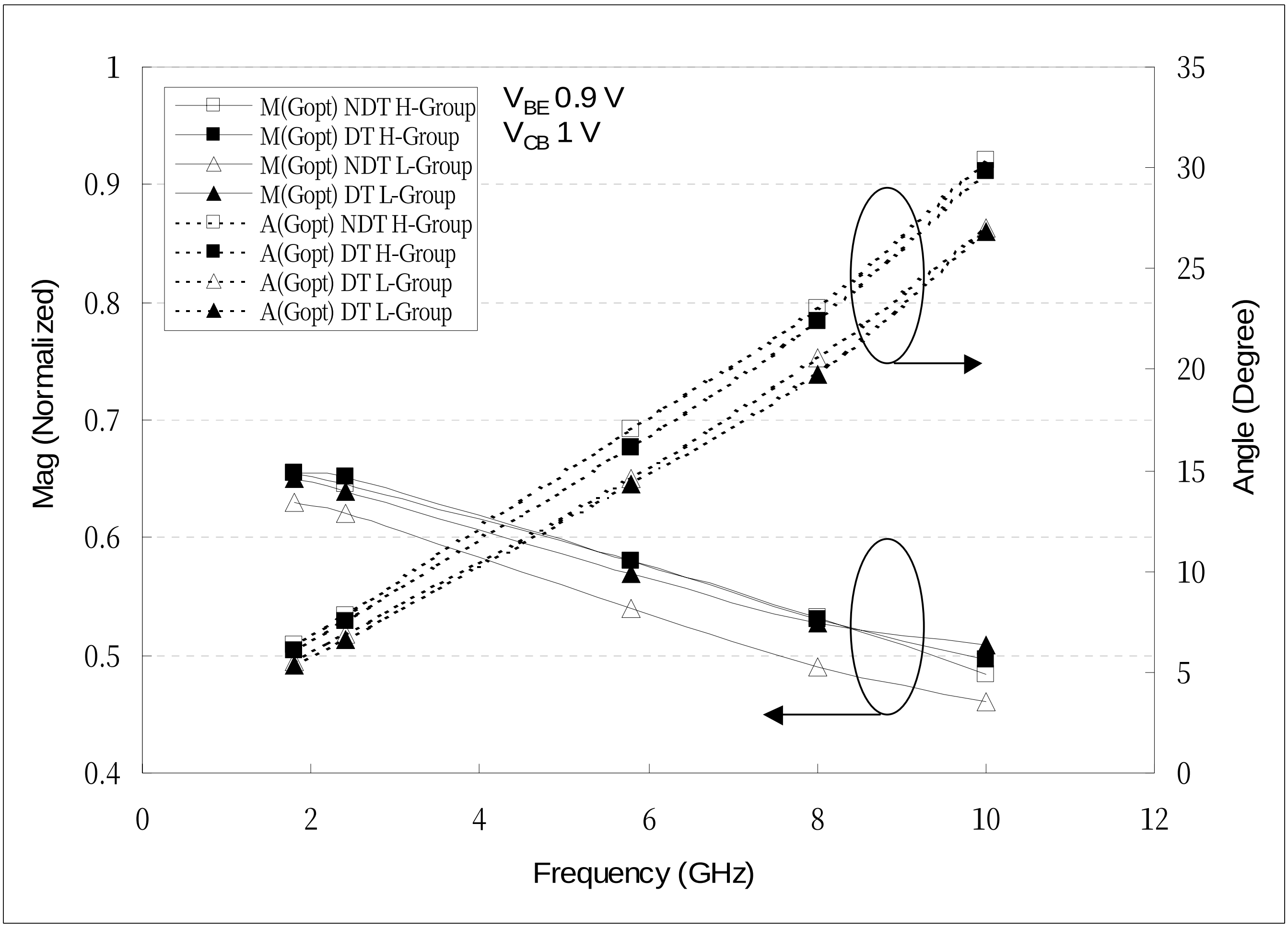

Magnitude and angle of Γ_{opt} of DT and NDT devices in H and L groups versus operation frequency at V_{BE} 0.9 volt

Figure 4.2.2 (b)

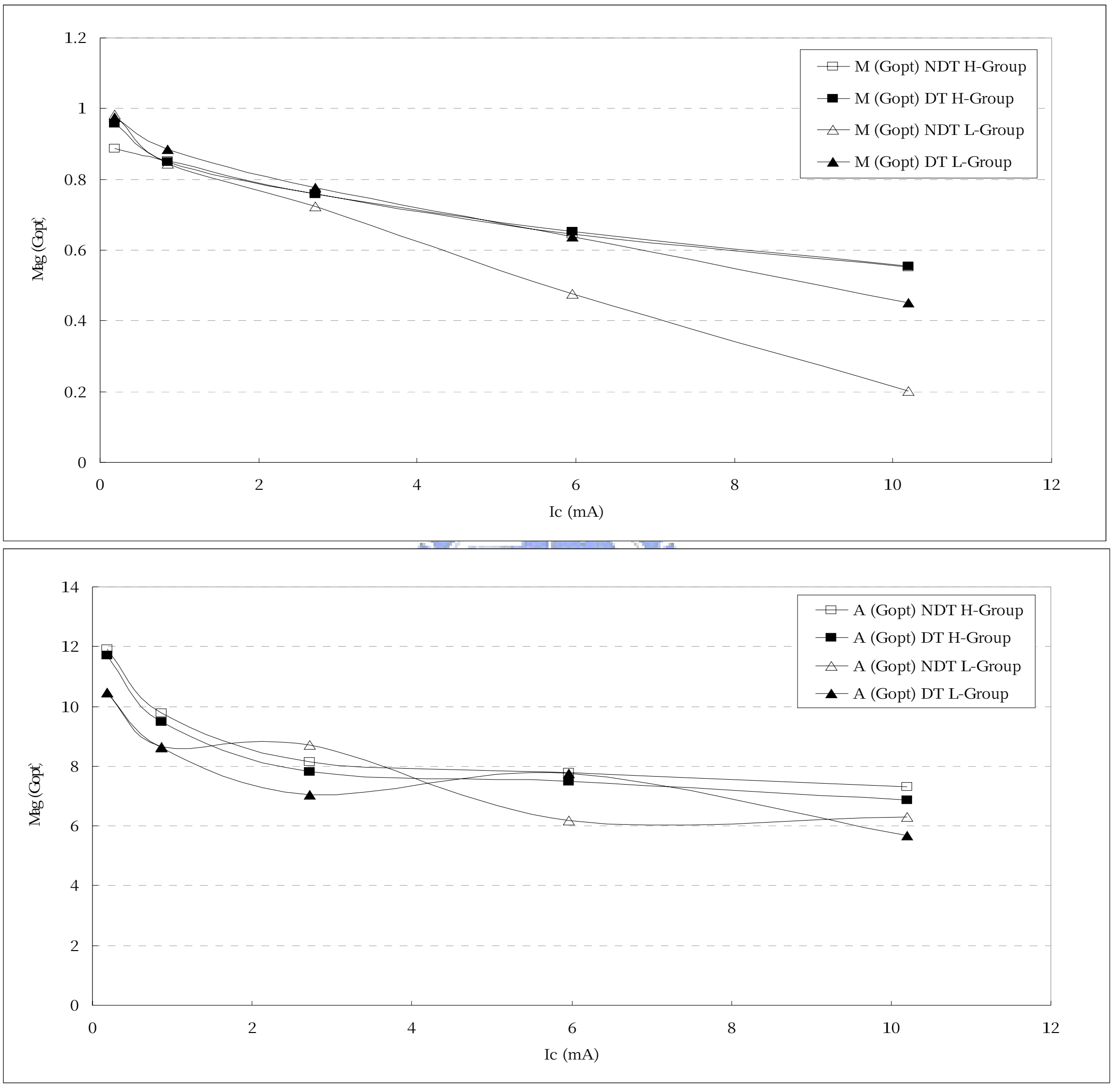

Magnitude and angle of Γ_{opt} of DT and NDT devices in H and L groups versus operation current at 2.4 GHz

Figure 4.2.2 (c)

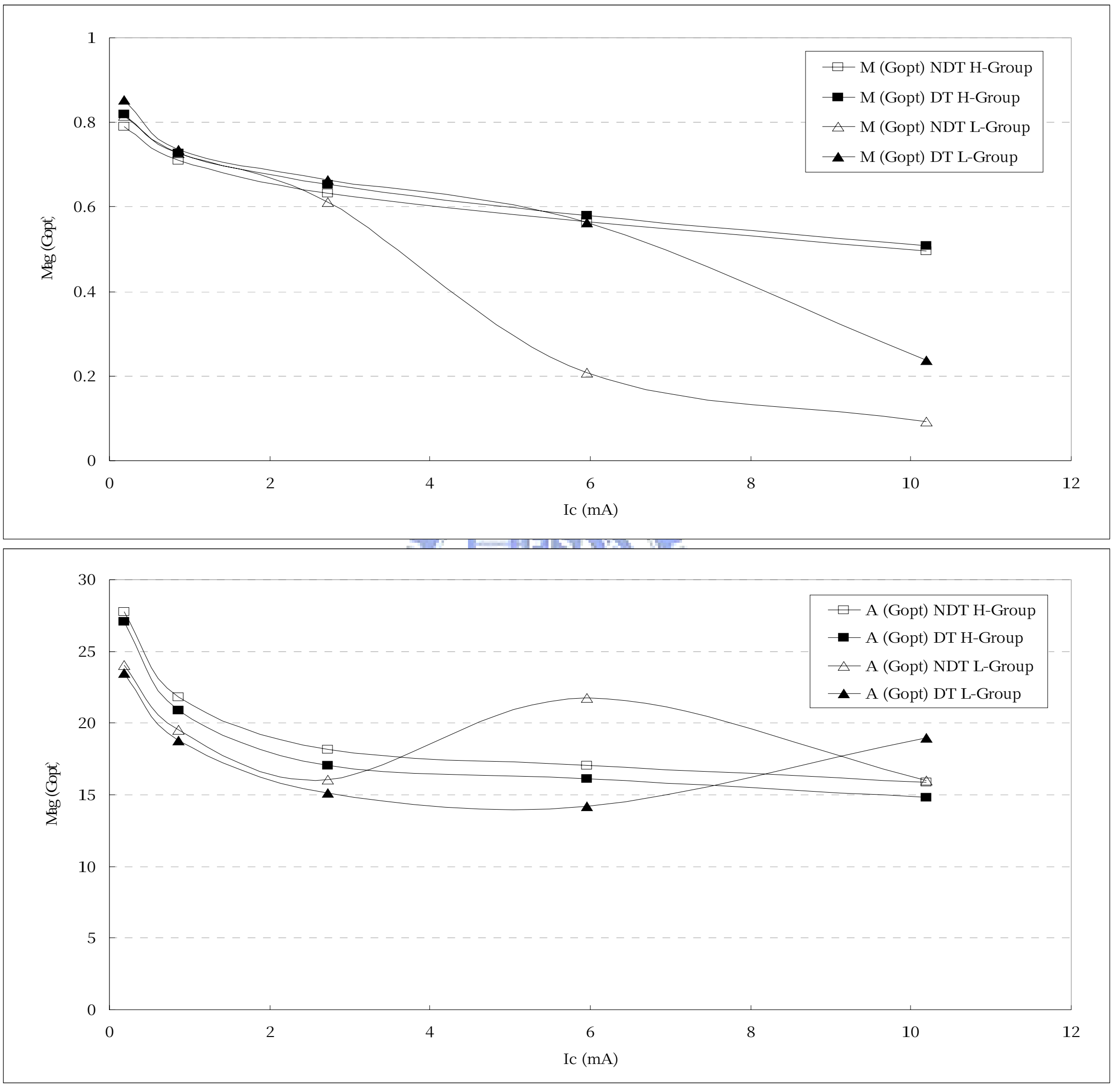

Magnitude and angle of Γ_{opt} of DT and NDT devices in H and L groups versus operation current at 5.8 GHz

Figure 4.2.2 (d)

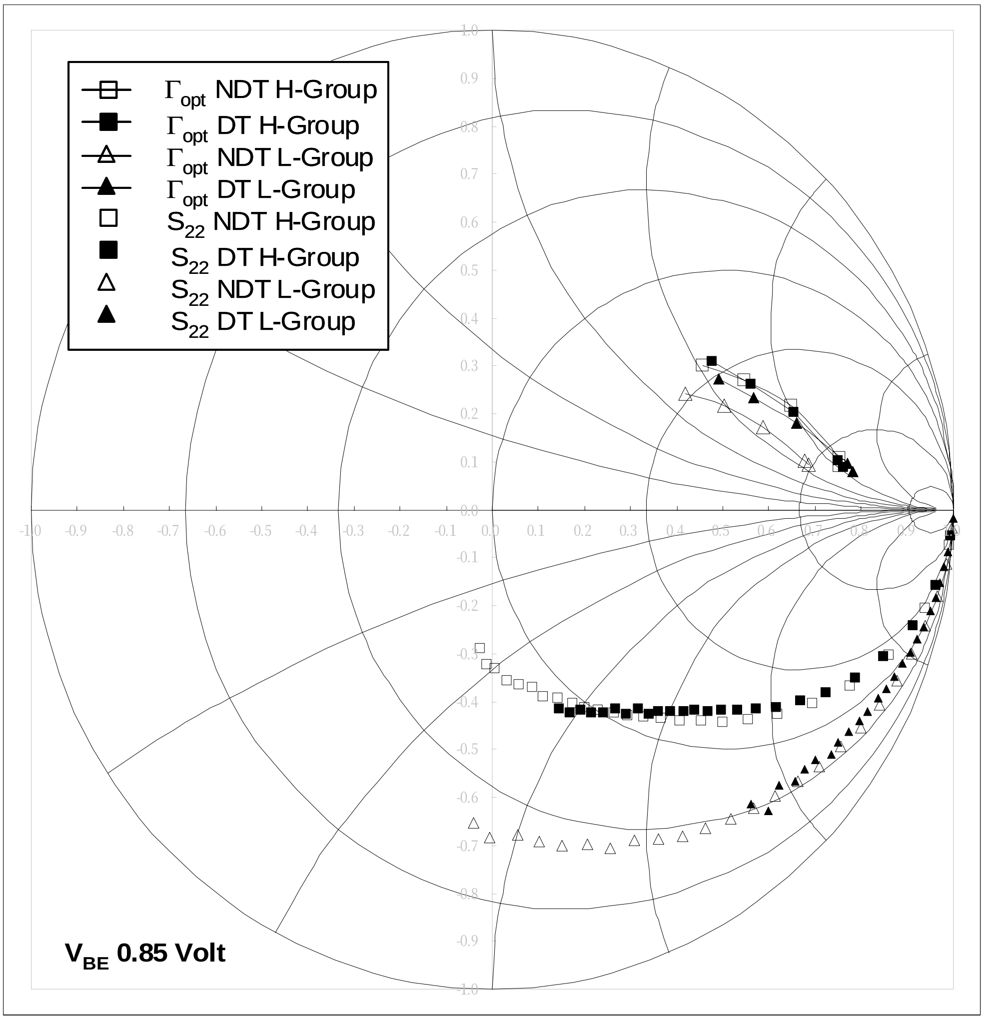

Γ_{opt} and S_{22} of DT and NDT devices in H and L groups versus operation frequency at V_{BE} 0.85 volt

Figure 4.2.3 (a)

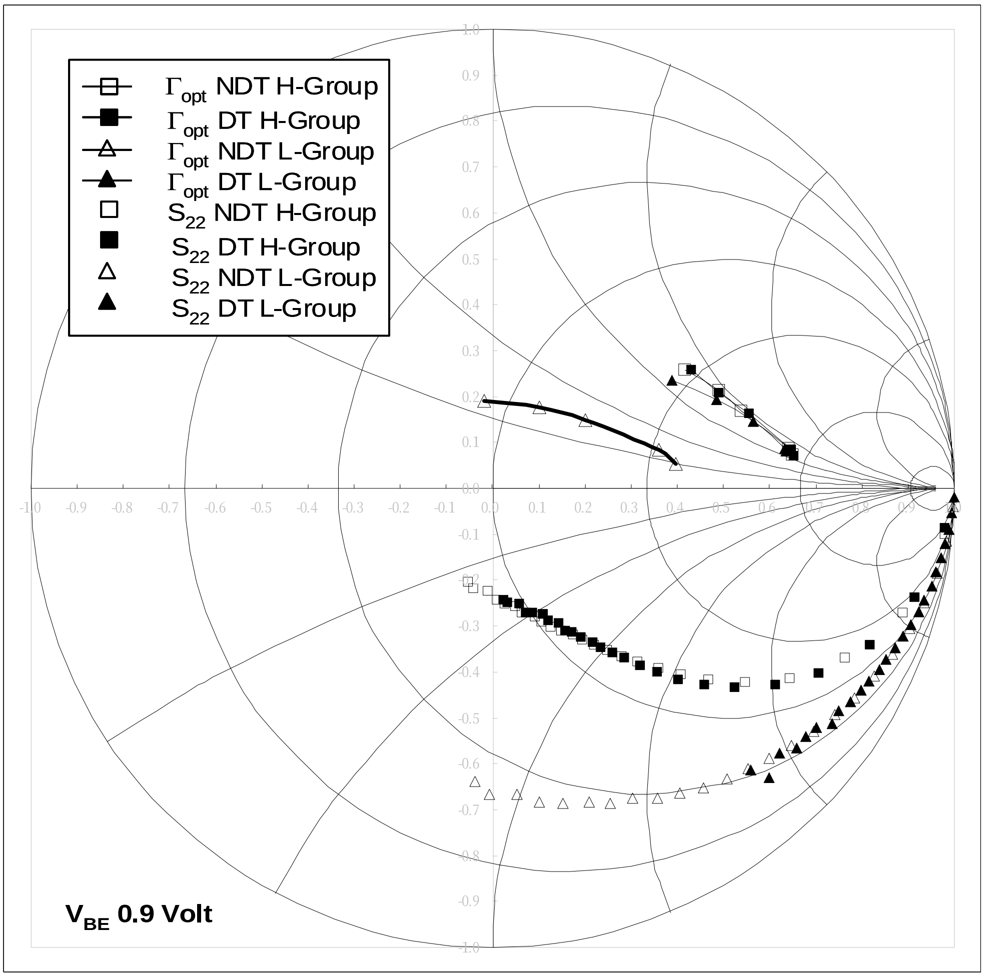

Γ_{opt} and S_{22} of DT and NDT devices in H and L groups versus operation frequency at V_{BE} 0.9 volt

Figure 4.2.3 (b)

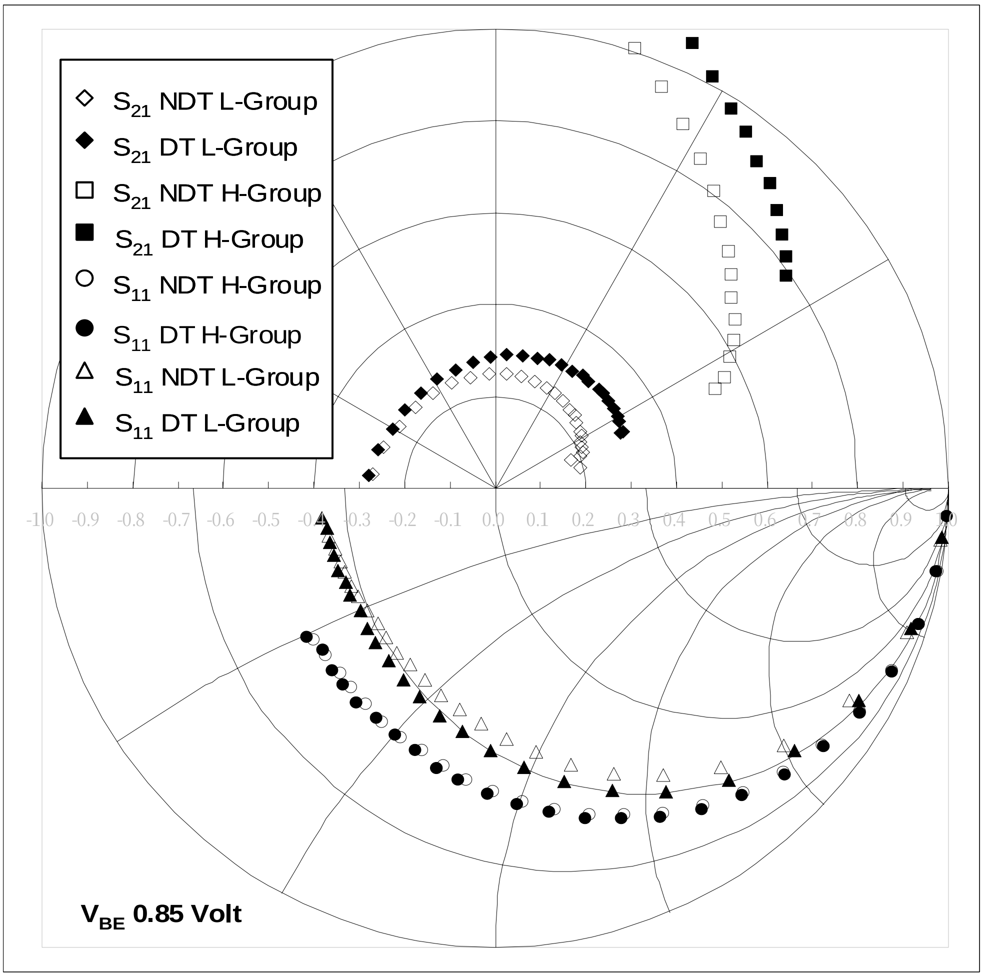

S_{11} and S_{21} of DT and NDT devices in H and L groups versus operation frequency at V_{BE} 0.85 volt

Figure 4.2.3 (c)

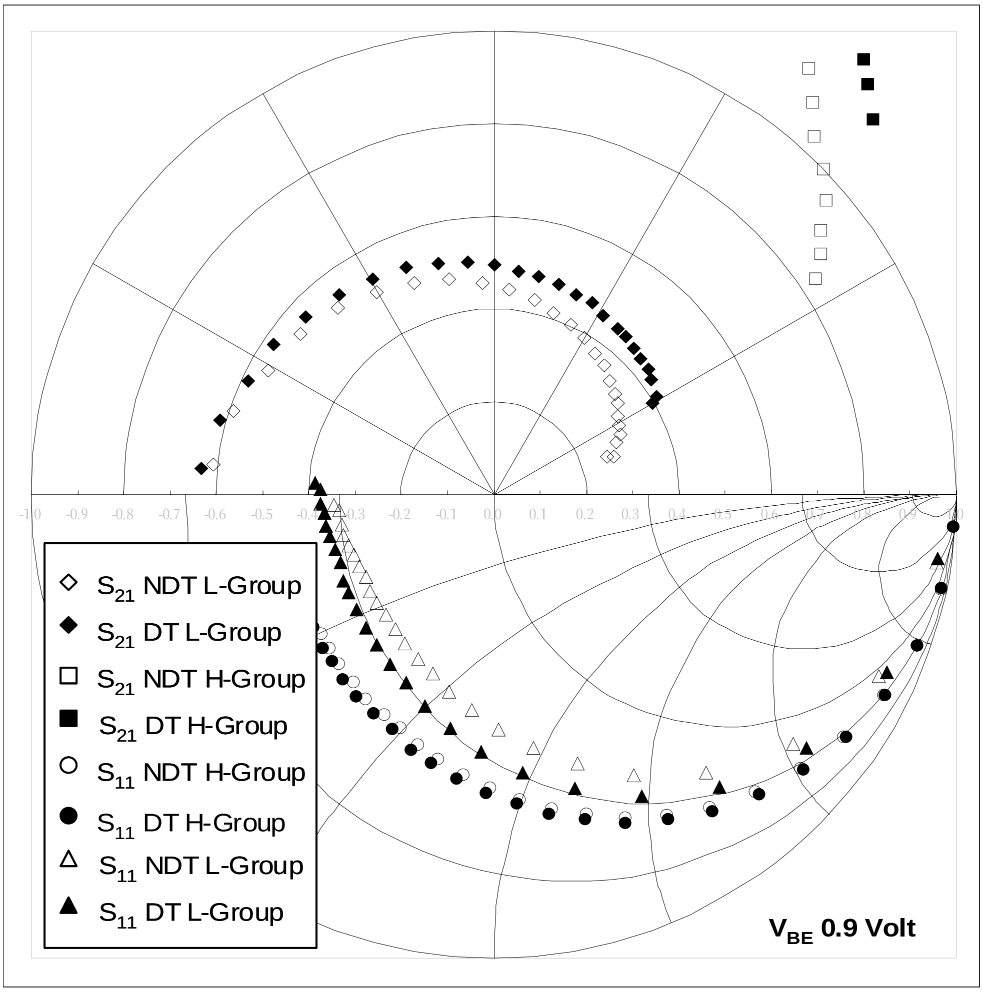

S_{11} and S_{21} of DT and NDT devices in H and L groups versus operation frequency at V_{BE} 0.9 volt

Figure 4.2.3 (d)

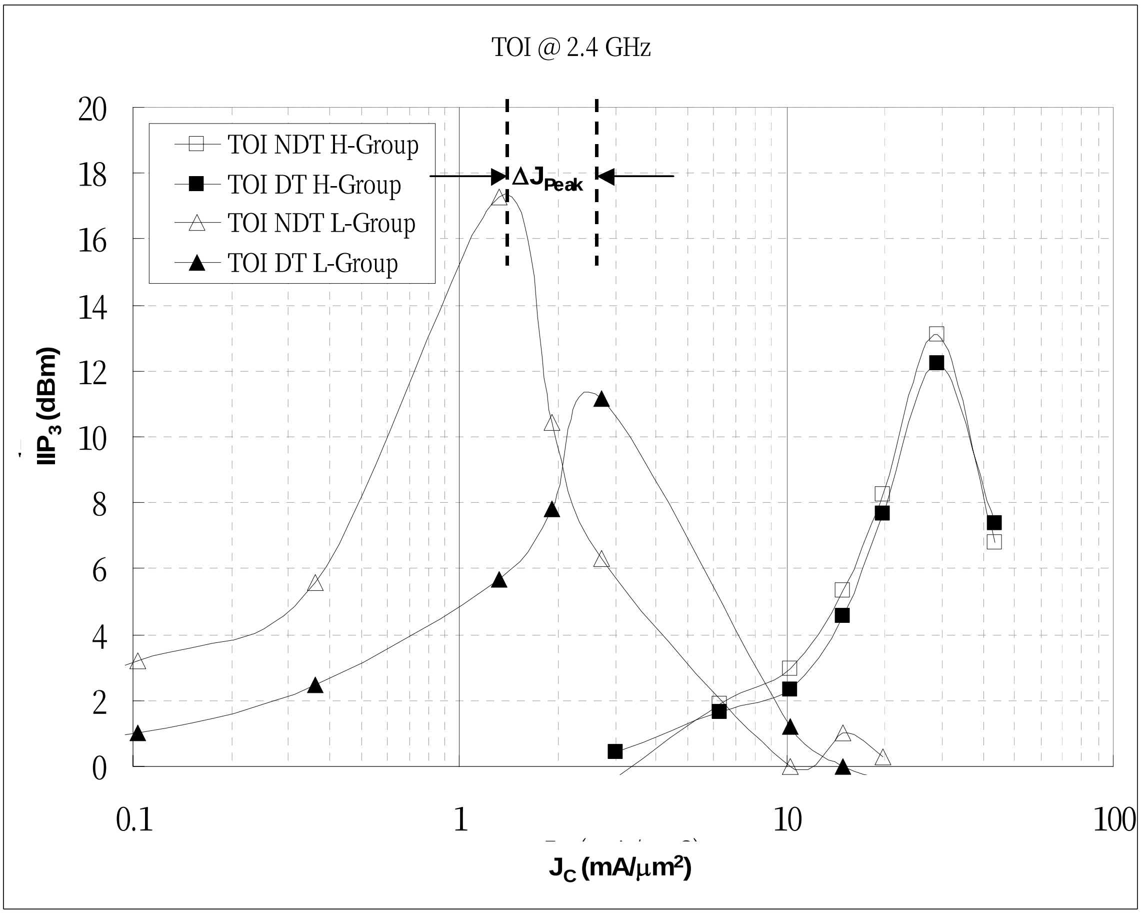

Third order intersect of HBT devices in H and L groups versus operation current at 2.4 GHz

Figure 4.3.1 (a)

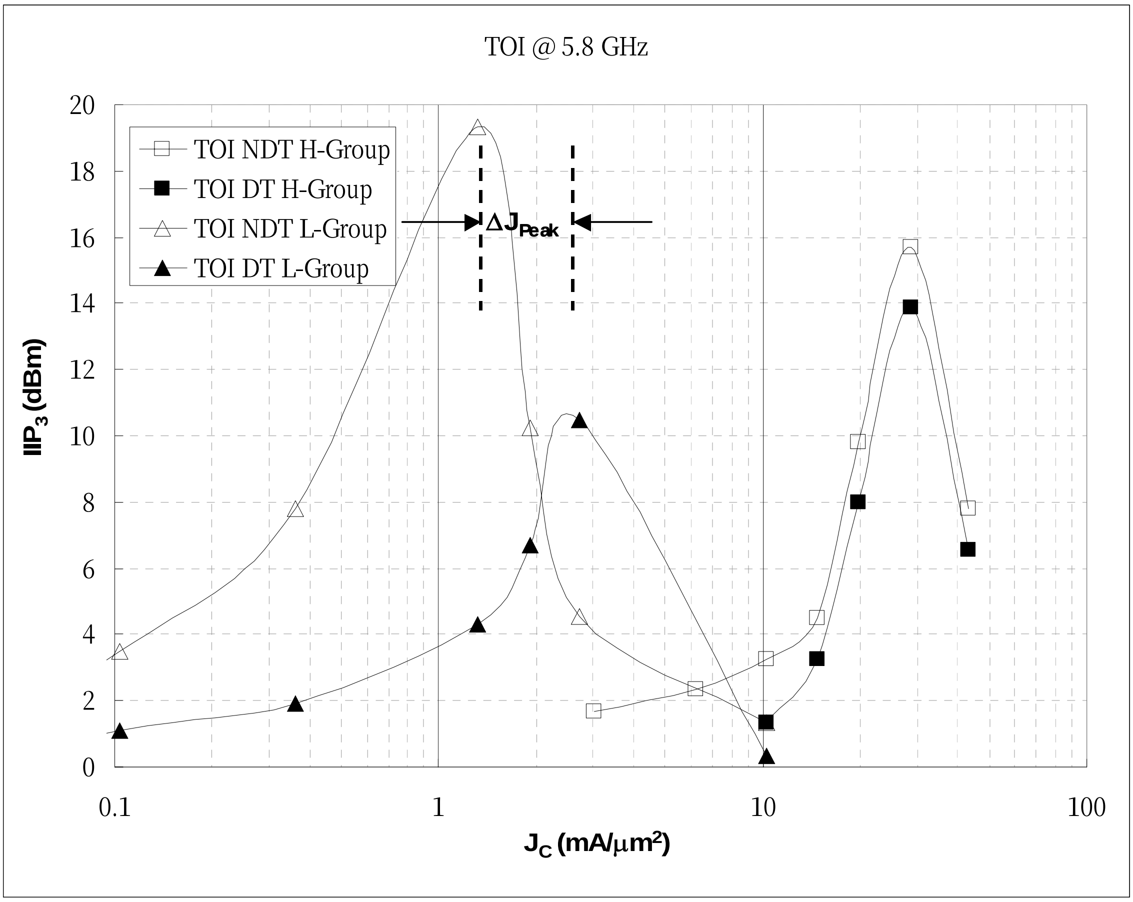

Third order intersect of HBT devices in H and L groups versus operation current at 5.8 GHz

Figure 4.3.1 (b)

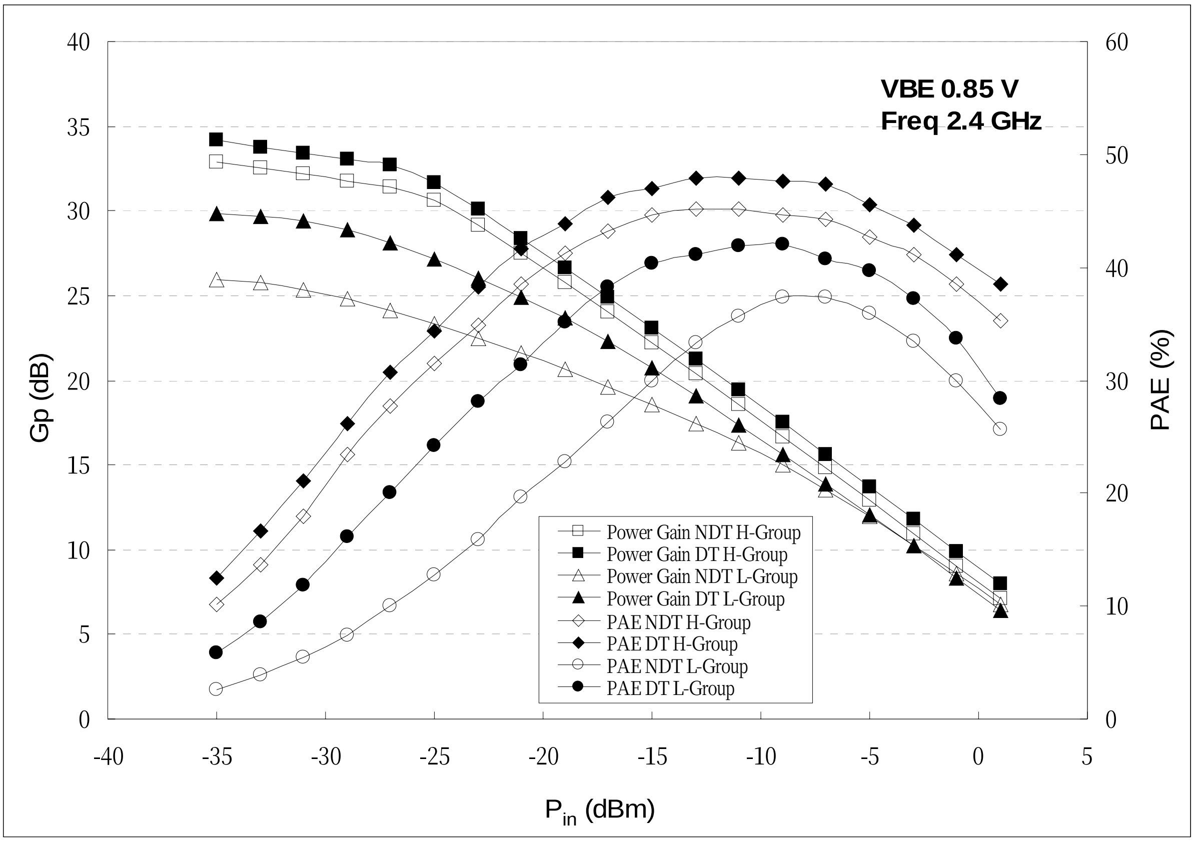

Third order intersect of HBT devices in H and L groups versus input power at VBE 0.85 volt and operation frequency 2.4 GHz

Figure 4.3.2 (a)

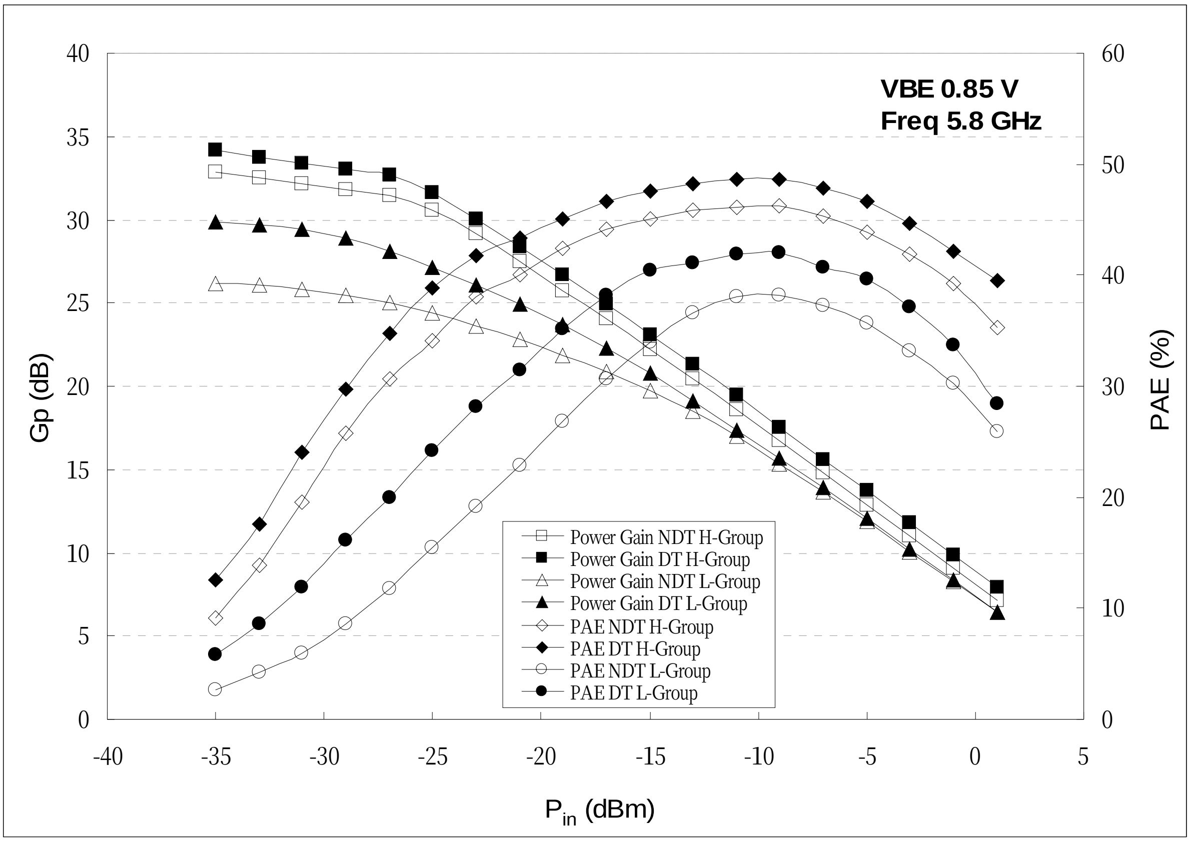

Third order intersect of HBT devices in H and L groups versus input power at VBE 0.85 volt and operation frequency 5.8 GHz

Figure 4.3.2 (b)

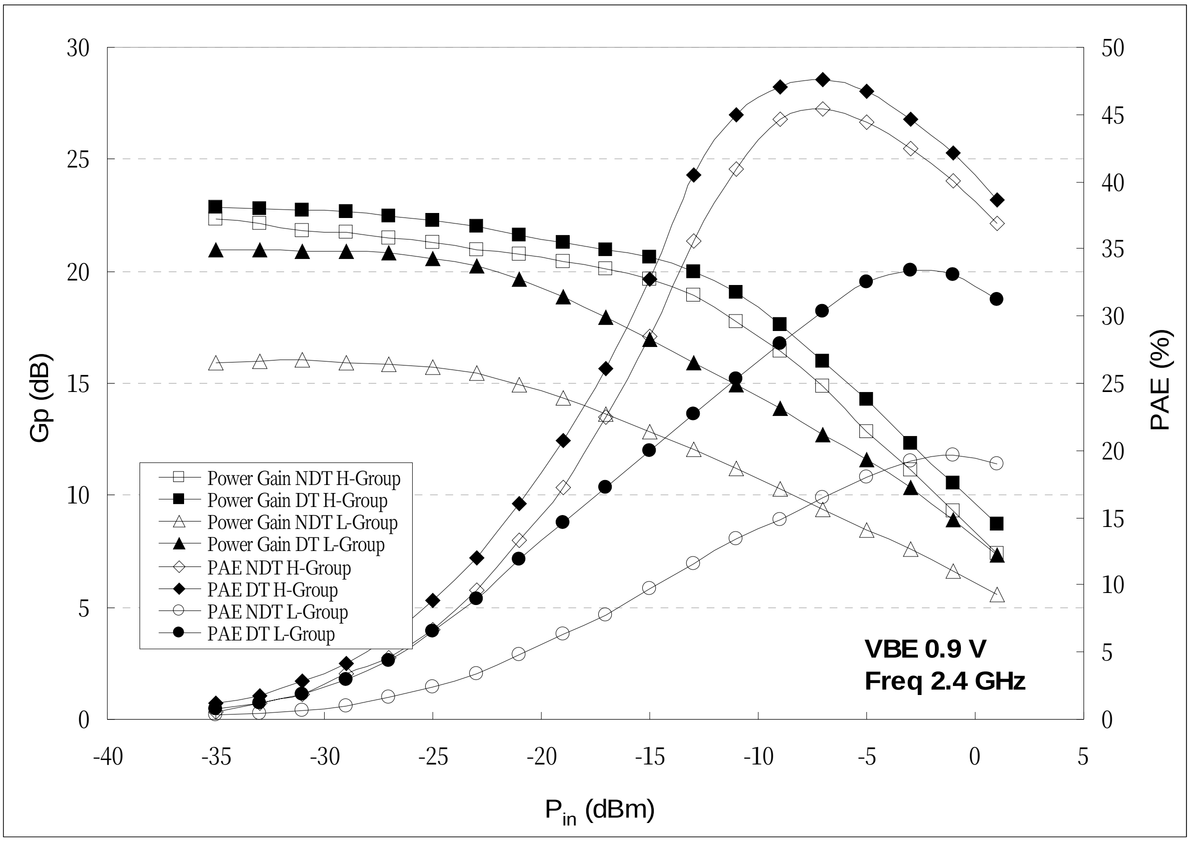

Third order intersect of HBT devices in H and L groups versus input power at VBE 0.9 volt and operation frequency 2.4 GHz

Figure 4.3.2 (c)

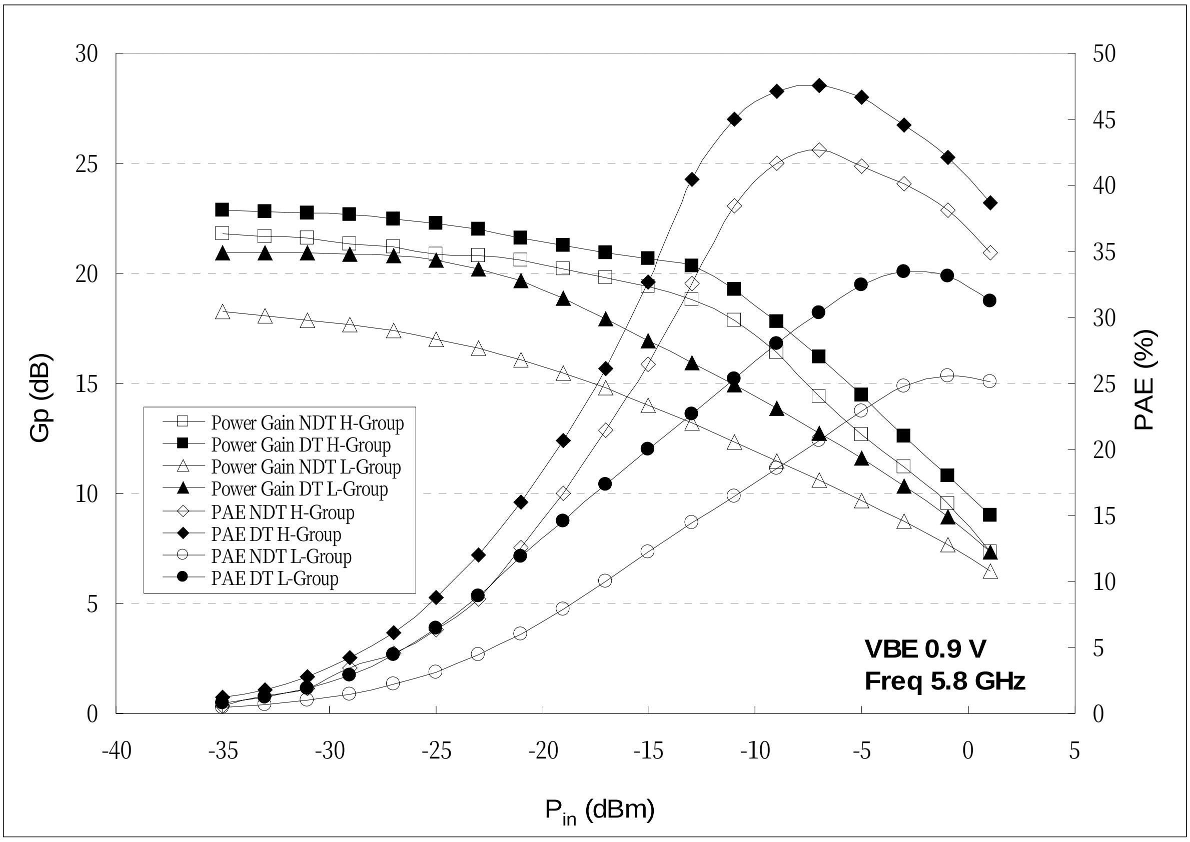

Third order intersect of HBT devices in H and L groups versus input power at VBE 0.9 volt and operation frequency 5.8 GHz

Figure 4.3.2 (d)